



Provided by the author(s) and University of Galway in accordance with publisher policies. Please cite the published version when available.

Title	Bi-frequency symmetry difference EIT - feasibility and limitations of application to stroke diagnosis
Author(s)	McDermott, Barry; O'Halloran, Martin; Avery, James; Porter, Emily
Publication Date	2019-12-19
Publication Information	McDermott, B. J., Ohalloran, M., Avery, J., & Porter, E. (2019). Bi-Frequency Symmetry Difference EIT - Feasibility and Limitations of Application to Stroke Diagnosis. IEEE Journal of Biomedical and Health Informatics, doi: 10.1109/JBHI.2019.2960862
Publisher	Institute of Electrical and Electronics Engineers (IEEE)
Link to publisher's version	https://dx.doi.org/10.1109/JBHI.2019.2960862
Item record	http://hdl.handle.net/10379/15663
DOI	http://dx.doi.org/10.1109/JBHI.2019.2960862

Downloaded 2024-04-23T19:08:37Z

Some rights reserved. For more information, please see the item record link above.



Bi-Frequency Symmetry Difference EIT – Feasibility and Limitations of Application to Stroke Diagnosis

Barry McDermott^{1,*}, Martin O'Halloran¹, James Avery² and Emily Porter¹

Abstract— Objective: Bi-Frequency Symmetry Difference (BFSD)-EIT can detect, localize and identify unilateral perturbations in symmetric scenes. Here, we test the viability and robustness of BFSD-EIT in stroke diagnosis. **Methods:** A realistic 4-layer Finite Element Method (FEM) head model with and without bleed and clot lesions is developed. Performance is assessed with test parameters including: measurement noise, electrode placement errors, contact impedance errors, deviations in assumed tissue conductivity, deviations in assumed anatomy, and a frequency-dependent background. A final test is performed using ischemic patient data. Results are assessed using images and quantitative metrics. **Results:** BFSD-EIT may be feasible for stroke diagnosis if a signal-to-noise ratio (SNR) of $\geq 60\text{dB}$ is achievable. Sensitivity to errors in electrode positioning is seen with a tolerance of only $\pm 5\text{mm}$, but a tolerance of up to $\pm 30\text{mm}$ is possible if symmetry is maintained between symmetrically opposite partner electrodes. The technique is robust to errors in contact impedance and assumed tissue conductivity up to at least $\pm 50\%$. Asymmetric internal anatomy affects performance but may be tolerable for tissues with frequency-dependent conductivity. Errors in assumed external geometry marginally affect performance. A frequency-dependent background does not affect performance with carefully chosen frequency points or use of multiple frequency points across a band. The Global Left-Hand Side (LHS) & Right-Hand Side (RHS) Mean Intensity metric is particularly robust to errors. **Conclusion:** BFSD-EIT is a promising technique for stroke diagnosis, provided parameters are within the tolerated ranges. **Significance:** BFSD-EIT may prove an important step forward in imaging of static scenes such as stroke.

Index Terms— electrical impedance tomography, reconstruction algorithm, stroke imaging

I. INTRODUCTION

RAPID and definitive stroke diagnosis is a vital clinical need. Specifically, a diagnosis must identify the underlying cause of the stroke, i.e., hemorrhagic lesion (bleed) or ischemic lesion (clot), prior to the initiation of tailored treatment [1], [2].

Currently diagnosis is by gold standard imaging modalities such as CT or MRI [3]. These technologies offer unparalleled sensitivity and specificity, with MRI for example offering near 100% sensitivity and specificity for hemorrhage [4] and circa 90% for ischemia in the acute stage [5]. However, the modalities suffer from issues related to cost and access: only 4-10% of stroke patients receive critical treatments like thrombolysis due to delay in access to imaging [6]. Technologies are needed that can accelerate the diagnosis of stroke in order to expediate treatment and improve outcomes.

Electrical Impedance Tomography (EIT) may represent such a technology. EIT is an imaging technology with many proposed biomedical applications. In EIT, electrodes are placed at the boundary of the domain of interest with alternating current injected, and voltage measured between pairs of electrodes according to a predefined protocol. The current used is at an innocuous safe level, limited by the IEC 60601-1 standard to amplitudes of the order of μA at frequencies up to 1 kHz, rising to a 10 mA limit for frequencies over 100 kHz [7], [8]. The resulting measurement frame can be used to reconstruct an image of the interior of the domain in terms of the electrical conductivity of the constituent tissues [8]. EIT represents a low-cost, portable, hazard free technology that may be capable of providing a diagnosis at the point of first patient contact and facilitate the initiation of time critical treatment. EIT may also support triaging stroke patients and expediate patients on the appropriate pathway.

There are challenges facing the translational of EIT into a device for such a clinical application. EIT is highly sensitive to a variety of errors (for example modelling errors in electrodes and boundary shape) with resulting contamination of the reconstructed image with artefacts [9]–[12]. As a result, time-difference EIT (tdEIT), where the use of a baseline measurement cancels out many time-constant errors, is the most commonly used modality [11]. However, tdEIT is not applicable when there is no change in the region of interest over

¹This paper was submitted on March 26, 2019. The research leading to these results has received funding from the European Research Council under the European Union's Horizon 2020 Programme/ ERC Grant Agreement BioElecPro n.637780, Science Foundation Ireland (SFI) grant number 15/ERCS/3276, the Hardiman Research Scholarship from NUIG, the charity RESPECT and the People Programme (Marie Curie Actions) of the European Union's Seventh Framework Programme (FP7/2007-2013) under REA Grant

Agreement no. PCOFUND-GA-2013-608728. J Avery was supported by the NIHR Imperial BRC.

*B. McDermott, M. O'Halloran and E. Porter are with the Translational Medical Device Lab, National University of Ireland Galway. J Avery is with The Department of Surgery & Cancer, Imperial College London, London, UK (correspondence e-mail: b.mcdermott3@nuigalway.ie).

time (i.e. no baseline measurement is available), as is the case in many biomedical applications.

In such static cases, alternative modalities of EIT are needed, such as absolute EIT (aEIT) and frequency-difference EIT (fdEIT). Imaging using aEIT is possible but highly sensitive to errors which other modalities mitigate to an extent by differencing frames [11], [13], [14]. In fdEIT measurements are taken at two or more frequencies with differencing, and error suppression is viable if there is a frequency-dependent change in the conductivity of the tissues [14]. However, fdEIT is generally more challenging than tdEIT [12]. Simple frequency-difference methods using linear reconstruction work well in the case of homogenous frequency-independent backgrounds (with a frequency-dependent perturbation) [15]. Weighted frequency-difference algorithms are capable of anomaly detection in simple inhomogeneous backgrounds, but performance degrades with more complex backgrounds, particularly when the background conductivity changes by more than 20% [15], [16].

Such ‘static imaging’ scenarios include stroke. Further, stroke diagnosis using EIT may face additional challenges. For example, the current reaching the brain from the electrodes on the scalp is severely attenuated by the highly resistive skull which limits the passage of current, as well as a layer of highly conductive cerebrospinal fluid (CSF) which acts to shunt current away [8]. The result is a low amplitude measured voltage due to the limited amount of current flowing through the brain. In [17], an EIT algorithm based on symmetry was presented where hemispheres were compared. While promising, the work of [17] used 2D numerical and phantom models of a perfectly symmetrical head, required knowledge of which side of the head was normal, and required duplication of isolated half measurement frames from each hemisphere to artificially complete a full measurement frame. A novel fdEIT algorithm by Malone *et al.* was described in [13] which used nonlinear methods and spectral constraints to achieve image reconstruction. When applied to the stroke problem in numerical studies, this spectrally constrained fdEIT algorithm was found to be highly sensitive to errors in electrode position (errors as low as 0.5 mm resulted in failure to detect lesions), reasonably robust to erroneous assumptions of tissue conductivity spectra (addressed in [12]) and highly robust to errors in contact impedance of electrodes. However, the model used did not include the CSF layer and was sensitive to artefacts due to errors in skull shapes [18]. Further, the algorithm was computationally expensive taking 5-6 hours for image reconstruction. Bleed detection was also found to be more challenging than clot detection, likely due to the relatively small change in contrast between the bleed and background across the range considered [18].

In order to advance the application of EIT to static lesion detection, we recently introduced the novel Bi-Frequency Symmetry Difference EIT (BFSD-EIT) algorithm [19]. This algorithm can be applied in situations featuring a plane of symmetry and where a perturbation causes a change in the (a)symmetry of the scene. Detection of changes in symmetry at two frequency points (f points) combined with *a priori* information of the expected tissues in the domain and the

frequency-dependent conductivities of these tissues can be used to detect, localize and identify lesions using reconstructed EIT images and key metrics [19]. Unlike [17], BFSD-EIT compares the entire head and the mirror image of the entire head, requires no knowledge of which side is normal, was developed on anatomically accurate 3D models with a degree of inherent normal asymmetry, and does not require duplication of parts of measurement frames. In this work, we study the feasibility of BFSD-EIT when applied to the stroke diagnostic problem. Specifically, we quantify the robustness and limitations of the algorithm to a range of errors. A series of numerical studies are conducted on a realistic, 4-layer head model, that feature different limiting scenarios and modelling errors. The situations addressed include the effects of:

- Measurement Frame Noise;
- Electrode Positioning Errors;
- Contact Impedance Errors of Electrodes;
- Assumed Conductivity Errors of the Tissues (including at a voxel level and whole tissue level);
- Errors in Assumed Anatomy of the Head (including skull, brain and scalp boundary);
- A Frequency-Dependent Background.

These error situations comprise some of the most common and important errors and challenges of EIT [10], [11], [14], [18]. The result of these tests indicates where the BFSD-EIT technique may be used, modifications that can be implemented to improve the outputs, parameter ranges that must be respected, and limitations of the algorithm when applied to stroke diagnosis. As a final test, BFSD-EIT is applied for the first time to data from a human ischemic stroke in order to assess performance in a real-world scenario.

The layout of the paper is as follows. In Section II the 4-layer numerical model is described, as well as an overview of the BFSD-EIT algorithm, and the key quantitative metrics used to assess performance. In Section III, the various test scenarios and results are reported, with these discussed in Section IV. The paper concludes with Section V, which also briefly compares the results of this work to the state-of-the-art in EIT for stroke diagnosis [13], [18].

II. MATERIALS AND METHODS

This section details the numerical models used as well as the methods for data generation using EIT, before presenting a summary of the BFSD-EIT algorithm, and the quantitative metrics applied to the reconstructions to then assess performance.

A. Numerical Model and Data Generation

This section describes the ideal (‘correct’) model without errors. The results described for this model are used to compare the performance of the algorithm applied to models with added errors (‘deviation’ models). Further, the model and methods described in this section are the basis of the deviation models.

The 4-layer numerical head model described in [19] was the basis for this study. The model was created from CT and MRI images of an adult patient, with anatomically accurate brain, CSF, skull and scalp layers incorporated. These four layers

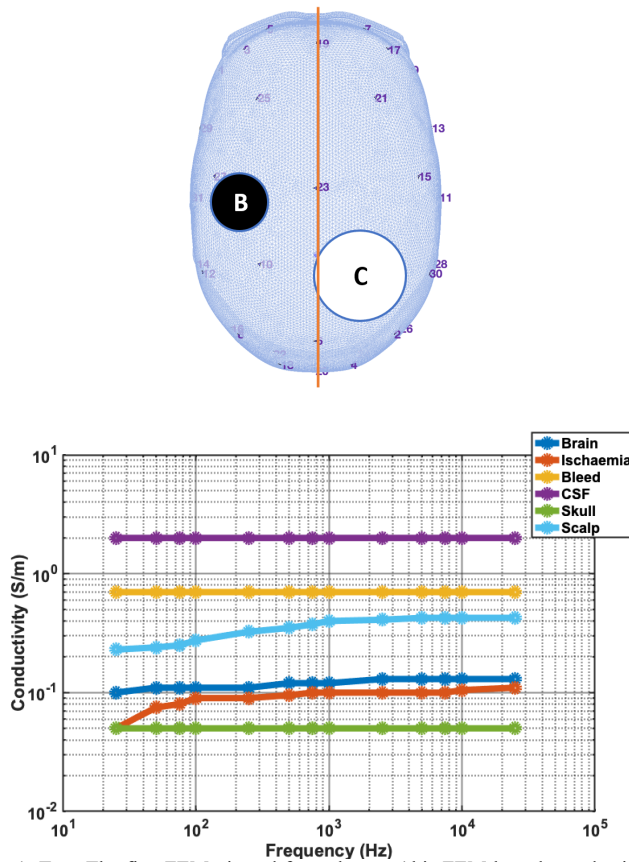


Fig. 1. Top: The fine FEM viewed from the top (this FEM has electrodes in A-Orientation). The sagittal plane is shown as an orange line. The positions of the two model lesions, a 10 ml spherical bleed ('B') and 50 ml spherical clot ('C') are shown. In a given case only one (or neither) of the lesions are present. Bottom: The conductivity spectra of the tissues of the modelled tissues from 25 Hz – 25 kHz (adapted from [16], [24]).

represent the most important anatomical layers for EIT applied to the head and are included in most state-of-the-art models [8], [20]. Importantly as the human head is not itself perfectly symmetric about the sagittal plane, the model used is also not perfectly symmetric. This asymmetry is quantified in [19], with for example the skull layer having a 90.1% degree of symmetry while the brain has 98.3%. Although the BFS-D-EIT algorithm is based on the principle of symmetry a degree of tolerance to normal asymmetry must be present. This model was used to simulate EIT forward and inverse problems using the finite element method in order to generate data [14].

A finite element method (FEM) model comprised of 4 million tetrahedrons was used as a fine mesh, forward solved to generate measurement frames with electrodes in one of two mirror image orientations (denoted A-Orientation and B-Orientation and described in more detail in the following subsection) (Fig. 1). A second coarse FEM mesh of 250,000 tetrahedrons used for image reconstruction in order to ensure independent models for both the forward and inverse (reconstruction) problems [21]. In total, 32 electrodes of diameter 10 mm and contact impedance 1 k Ω were modelled on the scalp [18], with symmetrical positioning across (or on) the sagittal plane. Refinement of a FEM near electrodes is recommended in general for EIT [22], but was not done in this study to facilitate a variety of errors models with minimal

alterations to the underlying mesh. Further, in all cases, comparison was made to results generated from the ideal model (also without mesh refinement).

The current injection protocol was designed to maximize the distance between electrode pairs. This protocol was used to generate measurement frames on the appropriate fine mesh using a parallel EIT forward solver (PEITS) [18], [19], [23]. The peak-to-peak current amplitude used was dependent on the frequency according to that allowed by IEC 60601-1 [7], with measurements taken at different frequencies (using different current amplitudes) objectively compared using appropriate gain adjustments.

The conductivity values of the tissues were derived from literature values [16], [24], and are provided in Fig. 1. For the test situations described in subsequent sections, the frequency (f) point of 25 Hz is used (unless noted). At this frequency, the conductivity of the tissues are 0.23 S/m, 0.05 S/m, 0.1 S/m, 2 S/m, 0.7 S/m and 0.05 S/m for scalp, skull, brain, CSF, bleed and clot respectively [16], [24], [25]. Further, three test cases are considered: that of no perturbation present ('N'), a 10 ml spherical bleed ('B') in a left mediolateral location and a 50 ml clot ('C') in a right posterolateral position (Fig. 1). A wide spectrum of lesion sizes is possible in stroke, with for example, the intracerebral hemorrhage volume in acute stroke reported in [26] as ranging from 1 – 101.5 ml (median 10.1 ml) and average infarction volume in acute stroke reported in [27] as 39.5 ± 84.9 ml.

B. Overview of BFS-D-EIT Algorithm

The BFS-D-EIT algorithm is described in detail in [19]. Briefly, the algorithm comprises of two steps:

(i) Detection of Deviation from Normal Symmetry:

The array of 32 electrodes on the scalp form symmetric electrode pairs. A measurement frame is taken in an "A-orientation" with a second frame taken in a mirror image "B-orientation". The B-orientation is made up of electrodes each of which is the symmetrical partner of the corresponding electrode in A-orientation. The injection protocol is the same in both orientations. EIT measurement frames are generated in both orientations at a pre-selected frequency point (f_i) with a difference image produced which can be used to detect deviations (or no deviation) in symmetry between the two orientations. This process allows lesion detection but not disambiguation (identification as bleed or clot) due to the presence of a confounding anti-lesion.

(ii) Disambiguation of Lesion Type:

The disambiguation step in BFS-D-EIT is based on analysis of the results from a second carefully chosen f point (f_2) where the conductivity (and more precisely contrast) between lesion and background change in different patterns for the two lesion types from f_i . The difference of change in contrast pattern between the lesions and brain that allows disambiguation.

A 0th order Tikhonov reconstruction onto the coarse mesh (corresponding to A-Orientation) using the input of the difference vector (Frame_B – Frame_A) results in a reconstructed image. Each voxel is assigned an intensity value proportional to the magnitude of the difference between the frames at that

location, with positive intensity values if the measurements from B-Orientation are more conductive than from A-Orientation at that location (negative in the opposite case). Difference vectors from the deviation models are similarly reconstructed onto this same coarse mesh derived from the ideal A-Orientation model.

BFS-D-EIT hence compares results from two f points. In [19], the f points of 25 Hz and 100 Hz were used with the 25 Hz point offering a high contrast in conductivity between clot and brain, as well as between bleed and brain. However, in this work the results at only a single f point are used to assess the feasibility of the algorithm (as accurate results from each f point is usually required for success). The high contrast between tissues at this frequency motivates the use of the 25 Hz point as the point of interest in this study. The limitations and robustness of the algorithm at one step to errors is representative of the robustness at both.

C. Definition of Quantitative Metrics

The reconstructions for the three test cases (illustrated in Fig. 2) are used to derive several quantitative metrics that can be used to support stroke diagnosis. The first key metric is the Global LHS & RHS Mean Intensity (GMI).

- GMI: The average intensity over all the voxels on each side (LHS and RHS) of the sagittal plane. The sign is represented as blue (negative) or red (positive) in the following figures while the magnitude is calculated to the \log_{10} . This metric alone was shown to detect, identify and localize a lesion (if present) in previous work [19].

Next, thresholding of the highest and lowest 5% of voxels by intensity (empirically chosen value) identifies contiguous voxels as candidate lesions. The largest remaining regions of interest (ROIs), one of both high and low intensity voxel sets, are then better isolated by further thresholding with only those voxels within the standard deviation of the mean intensity for each ROI kept and used to define ROI_H , ROI_L . This range of intensities are presented as the reconstructed images (Fig. 2). These ROIs are then filtered to remove ROIs within 10 mm of the mesh surface (assumed to be exterior to the brain or surface artefacts) and of volume < 5 ml (assumed to be below a reliable threshold volume for detection) [19]. Any remaining ROIs are then used to calculate the following metrics:

- ROI Mean Intensity (RMI): The mean intensity values of ROI_H and ROI_L with sign and magnitude represented in the same manner as the GMI. The values should follow the same pattern in terms of sign and relative magnitude to that of the GMI. In [19], it was suggested that the GMI may be more robust than RMI and in this work the RMI is similar (or less robust) to GMI in all cases and hence only the GMI is shown.
- Difference in Centroid Location (DCL): The difference in centroid location of ROI_H and ROI_L if one is reflected across the sagittal plane. Ideally $DCL = 0$ cm.
- Image Noise (IN): A measure of the number of thresholded voxels contained in the ROI compared to those in the entire thresholded image, averaged for the high (H) and low

intensity (L) voxel sets. Ideally $IN = 0$, with range $0 - 1$. The IN is given by:

$$IN = 1 - 0.5 \left(\frac{\Sigma(Voxels)_{ROI_H}}{\Sigma(Voxels)_H} + \frac{\Sigma(Voxels)_{ROI_L}}{\Sigma(Voxels)_L} \right). \quad (1)$$

- Morphology Deviance (MD): The degree of overlap between ROI_H and ROI_L if one ROI is reflected across the sagittal plane. Ideally $MD = 0$ (when perfect overlap occurs). The range of MD is $0 - 1$.

Where applicable, each test situation is iterated 10 times, each time with random variation of the error parameter within a chosen range (discussed in more detail in Section III). The mean and standard deviation of each of the above metrics are reported across the iterations. For iterated test situations, the Detection Rate is calculated:

- ROI Detection Rate (RDR): The percentage of times from the 10 iterations that ROIs are detected. Ideally the RDR is 0% for the N cases (no lesion present) and 100% for the B and C cases (where a lesion is present).

The GMI, RMI, DCL, IN and MD results for the ideal model cases are used to compare with subsequent deviation models with modelling errors. For brevity, deviation model metric results, and not reconstructed images, are reported in the following sections.

III. TEST SCENARIOS AND RESULTS

In this section the results of the ideal model test situations are reported followed by the results of the various deviation models. In total, 3 simulations were conducted for the ideal model tests with 265 simulations for the deviation models. A final test is also performed using human data.

A. Ideal Model Results

The reconstructed images and quantitative metrics from the ideal model for a simulation at a f point of 25 Hz are shown in Fig. 2. The reconstructed image for the N case is largely composed of artefacts at or near the mesh surface, while the images for the B and C cases show a significant reduction in these artefacts with the detected ROIs (due to the presence of a lesion) dominating the image. The GMI metric values have theoretically “equal but opposite” values regardless of the case. The N case give near zero values for GMI (LHS 0.33; RHS 0.38), indicating that both sides are symmetrically balanced and hence no lesion is present (or cannot be detected). The presence of a lesion deviates the GMI value away from zero with the magnitude a function of the size of the lesion, the lesion position, and the contrast between the lesion and brain. Case B (LHS 1.19; RHS 1.19) gives a higher GMI score compared to C (LHS 1.03; RHS 1.04) despite the smaller volume due to the closer proximity of B to the exterior and the greater contrast

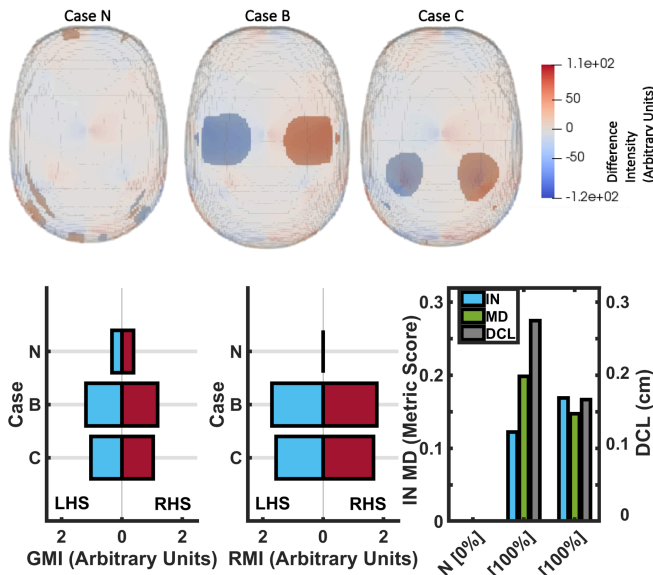


Fig. 2. Top: Reconstructed images of the ideal model for the three cases at an f point of 25 Hz: No lesion present (N); 10 ml spherical bleed in a left mediolateral location (B) and a 50 ml clot in a right posterolateral position (C). The N case shows noisy artefacts towards the exterior of the FEM whereas when a lesion is present the ROIs corresponding to the perturbation are the dominant feature. Bottom: Quantitative metrics corresponding to the reconstructed images. GMI: The blue bars represent a negative intensity value and the red bars a positive intensity value on either the LHS (negative x-axis) or RHS (positive x-axis). RMI: If no ROI is detected in a given case at a given frequency point, then no metric value is listed, the bars represent the RMI for the ROI_H (red bar) and ROI_L (blue bar) on either the LHS (negative x-axis) or RHS (positive x-axis). IN, MD and DCL: Are reported if ROIs are detected. The RDR for each case is reported on the x-axis of the IN, MD, DCL plot.

between blood and brain compared to clot and brain. Both lesions cause a mean negative intensity on the LHS and a mean positive intensity on the RHS demonstrating the need for disambiguation (as described in [19]).

For calculation of all metrics other than GMI, the ROI detection process is applied. In the N case, no lesion is present and no ROIs are identified, as expected. For both B and C, ROIs are successfully detected. In these cases, the RMI score gives the mean intensity of each of ROI_H and ROI_L with the pattern of values similar to the GMI (larger if larger lesion, nearer the exterior, larger contrast compared to brain). The DCL metric is < 3 mm for both cases indicating a high degree of overlap between the ROIs. The IN and MD values for the ideal cases (all < 0.2) can be used to compare to deviation models.

B. Measurement Frame Noise

In this test scenario, the measurement frames for each case at the f point of 25 Hz in each orientation were contaminated with additive Gaussian white noise at levels of 80 dB, 60 dB and 40 dB signal-to-noise ratio (SNR) before reconstruction. Illustrative quantitative metrics are shown in Fig. 3 for the 80 dB and 60 dB tests, with the RDR results shown for all noise levels.

The GMI results at 80 dB are comparable to the ideal results (i.e., SNR = ∞) from Fig. 2. However, the MD and DCL now increases for both cases B and C. At 60 dB, further degradation in performance is seen with deviations in GMI from the ideal,

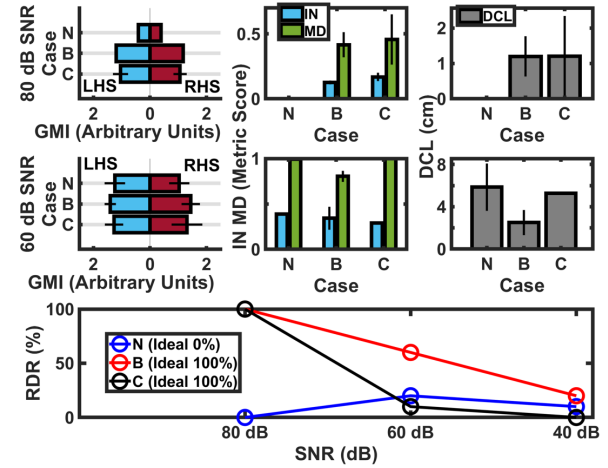


Fig. 3. Quantitative Metrics for models where noise of 80 dB, 60 dB and 40 dB SNR is added to the measurement frames prior to reconstruction for cases N (no lesion present); B (bleed); C (clot). GMI: The blue bars represent a negative intensity value and the red bars a positive intensity value on either the LHS (negative x-axis) or RHS (positive x-axis). IN, MD and DCL: Are reported if ROIs are detected. The RDR for each case is reported at each noise level. For the 40 dB models, the RDR is shown, but the excessive noise hinders the ability to detect ROIs.

increases in the size of the standard deviations (reported as error bars), large IN, MD, DCL metrics and detection of ROIs in the N case as well as failure to detect ROIs in the B and C cases (particularly evidenced by the 10% RDR for C). At 40 dB, excessive noise results in a common failure to detect lesions.

C. Electrode Positioning Errors

Two scenarios of erroneous electrode positioning are analyzed, where errors are present in the forward model relative to the inverse model and either: (1) symmetry is not maintained between symmetric electrode pairs; (2) symmetry is maintained between symmetric electrodes pairs. In both scenarios the goal was to find, and surpass, the point where the integrity of the results is maintained.

1) Electrode Positioning Errors with Symmetry Lost

The electrode centers are positioned randomly within a given radius of the ideal center position. No attempt is made to keep electrode pairs symmetric. The tested deviations in electrode positions were assigned with error radii of 1 mm, 2 mm, 5 mm, 10 mm, and 20 mm. The error radius for a model is the maximum distance an electrode can be positioned from the correct position on the mesh surface. Table I lists the distance error of the 32 electrodes in each model (averaged over the 10 repetitions) from the ideal position (and between electrode pairs). The quantitative metrics resulting from these test cases are provided in Fig. 4(a). The results indicate reliable performance (i.e. similar to the results achieved with the ideal model) for error radii of up to ± 5 mm if considering the GMI, but up to only ± 1 mm for the other metrics, with no ROIs reliably detected beyond this error radius (note the steep drop off in RDR for cases B and C).

2) Electrode Positioning Errors with Symmetry Maintained

In this series of test scenarios, the electrodes centers are positioned randomly within a given radius away from the ideal position. However, unlike in the previous section, now electrode pairs are kept symmetric with respect to each other across the sagittal plane (i.e. if reflected across the sagittal plane the electrodes map onto their partner exactly). The deviations tested were error radii of 2 mm, 5 mm, 10 mm, 20 mm, 30 mm, 40 mm and 50 mm. Hence electrodes are positioned at or within these error radii from the ideal position on the mesh surface. Table I lists the distance error of the 32 electrodes in each model from the ideal position (and between symmetric electrode pairs); the corresponding quantitative metrics are presented in Fig. 4(b).

The results indicate integrity of the BFSD-EIT algorithm is maintained up to the ± 20 mm error radius if considering the GMI (i.e. are largely similar to the ideal model, but for the other metrics only up to ± 5 mm, with no or erroneous ROIs detected beyond this error radius. Both results are improvements over the situation where symmetry is not maintained, suggesting that the BFSD-EIT algorithm can tolerate larger errors in expected electrode location if electrode pairs are kept symmetrical across the sagittal plane. Maintaining such a symmetry should be feasible to this degree in a clinical case, for example using an EEG cap for electrode placement [18].

D. Contact Impedance Errors of Electrodes

In this section, the impact of an inaccurate electrode contact impedance is investigated. In the ideal model, the electrode contact impedance is 1 k Ω .

Here, the impedance on each electrode is randomly set between 800 – 1200 Ω (1 k $\Omega \pm 0$ -20%) for a first test, and then within 500 – 1500 Ω (1 k $\Omega \pm 0$ -50%) in a second test. Further, each of these tests is conducted in two different ways, either with: (1) symmetry not maintained between electrode pairs (all electrodes have random contact impedances within the range);

TABLE I

MEAN \pm STANDARD DEVIATION OF THE DISTANCE ERRORS OF THE 32 ELECTRODES (SYMMETRY LOST OR SYMMETRY MAINTAINED)

Error Radius (mm)	Mean (mm) \pm Standard Deviation (mm) Of Electrode Positions with respect to the Correct Positions	Mean (mm) \pm Standard Deviation (mm) Of Distances between Symmetric Electrode Pairs (i.e. if reflected across the sagittal plane)
<i>Symmetry Lost</i>		
± 1	0.47 ± 0.34	0.64 ± 0.45
± 2	1.34 ± 0.21	1.52 ± 0.65
± 5	3.31 ± 0.34	3.88 ± 1.59
± 10	6.39 ± 0.78	7.84 ± 3.15
± 20	13.19 ± 1.41	15.64 ± 6.51
<i>Symmetry Maintained</i>		
± 2	1.21 ± 0.24	0 ± 0
± 5	3.21 ± 0.52	0 ± 0
± 10	6.33 ± 1.05	0 ± 0
± 20	13.39 ± 2.19	0 ± 0
± 30	19.03 ± 3.77	0 ± 0
± 40	24.39 ± 3.36	0 ± 0
± 50	31.32 ± 5.29	0 ± 0

(2) symmetry maintained (electrode pairs have the same erroneous impedance). Fig. 5 shows the resulting quantitative metrics for all of these scenarios. As can be observed from the figure, the results show that the lesion detection is effectively equivalent to that of the ideal scenario, for both impedance error levels, and regardless of whether symmetry is maintained or not.

E. Assumed Conductivity Errors of the Tissues

This section explores the impact of error on the assumed conductivities of the tissues. In the ideal model, the conductivities of the tissues are assigned as 0.23 S/m, 0.05 S/m, 0.1 S/m, 2 S/m, 0.7 S/m and 0.05 S/m for scalp, skull, brain, CSF, bleed and clot, respectively, at the f point of 25 Hz. Here, errors of $\pm 5\%$, $\pm 20\%$ and $\pm 50\%$ are added to each of these conductivity values in separate deviation models. These deviation models incorporate these errors on either: (1) a voxel

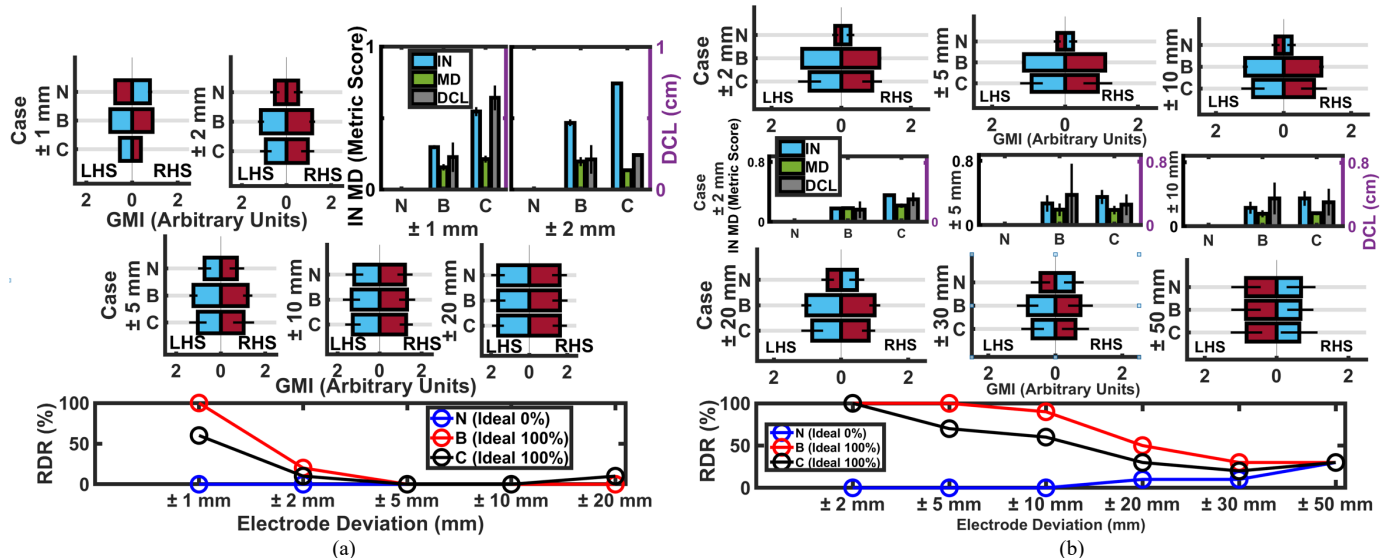


Fig. 4. Quantitative Metrics for erroneous electrode position models with symmetry lost (a), and symmetry maintained (b), between electrode pairs for cases N (no lesion present); B (bleed); C (clot). GMI: The blue bars represent a negative intensity value and the red bars a positive intensity value on either the LHS (negative x-axis) or RHS (positive x-axis). IN, MD and DCL: Are calculated if ROIs are detected and are shown for the situations. The RDR for each case is reported at each electrode deviation.

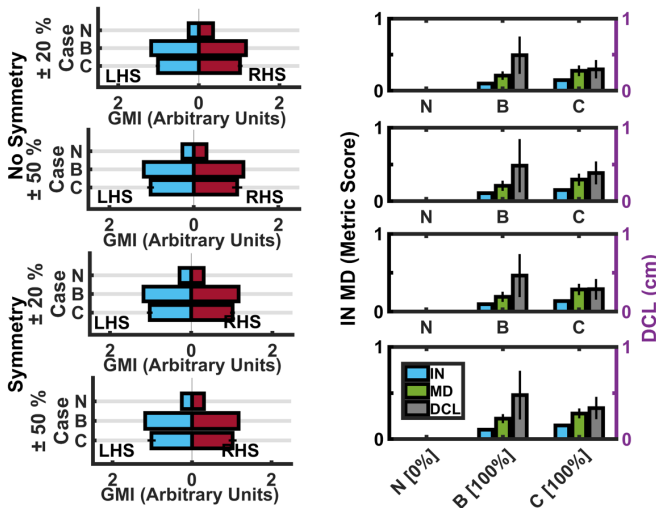


Fig. 5. Quantitative Metrics for erroneous electrode contact impedance models with (top 2 rows) No Symmetry: all electrodes have random contact impedances within the range $\pm 20\%$ or $\pm 50\%$; and (bottom 2 rows) Symmetry: symmetrical partner electrodes have the same (but erroneous) contact impedance within the range $\pm 20\%$ or $\pm 50\%$. Cases are N (no lesion present); B (bleed); C (clot). GMI: The blue bars represent a negative intensity value and the red bars a positive intensity value on either the LHS (negative x-axis) or RHS (positive x-axis). IN, MD and DCL: Are reported if ROIs are detected. The RDR for each case is reported on the x-axis of the IN, MD, DCL plot. The RDR for each case is reported on the x-axis of the bottom-most IN, MD, DCL plot and was identical (and ideal) in all deviation models tested

level, or (2) a whole tissue level.

There is evidence in the literature that the conductivity of the tissues of the head may be largely symmetric in the absence of pathology [28], [29]. However, the dielectric properties of tissues have a band of uncertainty around the reference values and may vary inter- and intra-patient [30]. Many factors such as natural heterogeneity in tissue, precise location, age, metabolic activity, pathology and the measurement method affect the measured conductivity of a tissue and result in a degree of variability in the assumed reference value [31], [32]. This uncertainty is even more pronounced at frequencies under 1 MHz (the region of interest for EIT) with significant variability in the dielectric properties of tissues, for example $\pm 24\%$ for fat and $\pm 35\%$ for blood [30], [33]. The choice of error values up to $\pm 50\%$ of the ideal value was motivated by these reported variability ranges from the literature.

1) Voxel Level Errors in Assumed Conductivity

In this test scenario, each voxel, corresponding to a discrete tissue, has a conductivity value assigned as the ideal conductivity of the tissue \pm an error which is up to 5, 20, or 50%, depending on the model. Each tissue is thus made heterogeneous while the ideal model assumes them to all be homogenous. The results are effectively identical to the ideal model results even up to and including an error of $\pm 50\%$ of the assumed tissue conductivity values (GMI results of $\pm 50\%$ shown in Fig. 6).

2) Whole Tissue Level Errors in Assumed Conductivity

In this test scenario, each voxel, corresponding to a discrete tissue, has a conductivity value assigned as the ideal

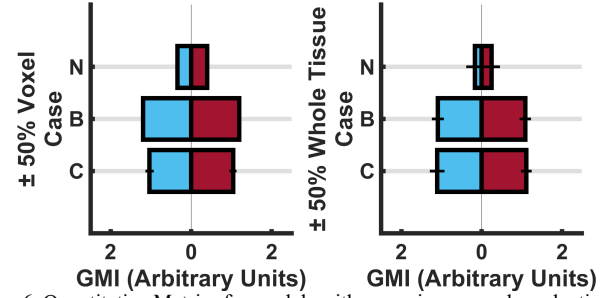


Fig. 6. Quantitative Metrics for models with errors in assumed conductivity of tissues. Each individual voxel corresponding to a given tissue (left) or the whole tissue (right) (scalp, skull, brain, CSF, bleed or clot) is assigned a conductivity corresponding to the ideal conductivity of that tissue \pm up to a maximum of 50% error. Cases are N (no lesion present); B (bleed); C (clot). GMI: The blue bars represent a negative intensity value and the red bars a positive intensity value on either the LHS (negative x-axis) or RHS (positive x-axis).

conductivity of the tissue \pm an error which is up to 5, 20, or 50%, depending on the model. Each tissue is thus made heterogeneous while the ideal model assumes them to all be homogenous. The results are effectively identical to the ideal model results even up to and including an error of $\pm 50\%$ of the assumed tissue conductivity values (GMI results of $\pm 50\%$ shown in Fig. 6).

F. Errors in Assumed Anatomy of the Head

BFS-D-EIT must be robust to a degree of anatomical asymmetry across the sagittal plane as well as deviations in the geometries of the fine (forward solved) and coarse (reconstruction) FEM meshes. In this section, two scenarios of anatomical deviations are considered: (1) Excess skull or brain on one side of the head with respect to the other; (2) Deviations in the geometry of the scalp (i.e. the boundary) between the fine and coarse meshes. In both scenarios, fine meshes are created with the altered anatomy, with reconstruction onto the ideal coarse mesh.

1) Unilateral Excess of Skull or Brain

As described in [19], the ideal model is based on an actual human head and is thus not perfectly symmetrical. The overall global symmetry of the head across the sagittal plane is calculated as the average percentage of voxels from each side that, when reflected across the sagittal plane, overlap with the voxels of that tissue type on the other side. For the ideal model, the global symmetry ranges from 90.1% for skull tissue to 98.3% for brain tissue. However, the ideal model does not have any gross asymmetry that may resemble a lesion.

Previous works have quantified the typical degree of asymmetry found in the skull [34] and brain [35]. An asymmetry index (AI), defined in [34]

as:

$$AI = \frac{RHS - LHS}{RHS} \times 100, \quad (2)$$

where RHS and LHS are the distances of a series symmetrical points on the right-hand side (RHS) and left-hand side (LHS) to a point on the sagittal plane, can be used to quantify the level of symmetry. The AI varies depending on person, cohort and anatomical location, but values of 3-6% have been reported

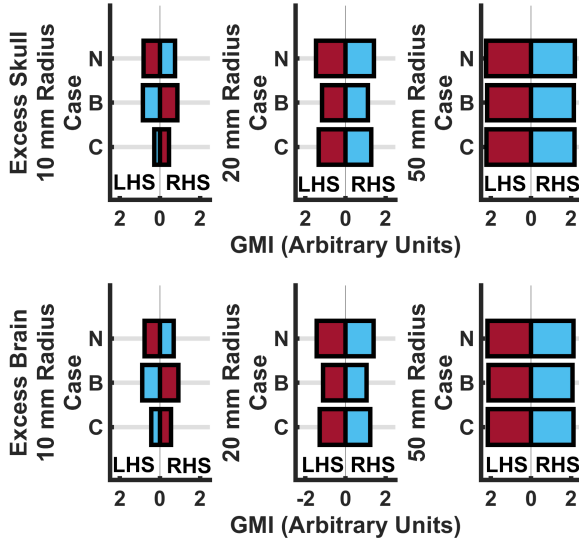


Fig. 7. Quantitative Metrics for models with excess skull (top row) or brain (bottom row) on the LHS compared to the RHS. In each model, the CSF encompassed by a sphere of radius 10 mm, 20 mm or 50 mm centred at a point on the LHS of the skull (or brain) is re-assigned as skull (or brain). Cases are N (no lesion present); B (bleed); C (clot). GMI: The blue bars represent a negative intensity value and the red bars a positive intensity value on either the LHS (negative x-axis) or RHS (positive x-axis).

[34].

For this study, an arbitrary location was selected on the left-hand side of the skull (or brain) at the approximate midpoint of the boundary between the frontal and temporal bones (lobes) on the left lateral interior surface (or exterior surface for the brain). Centered at this point, spheres of radii 10 mm, 20 mm, and 50 mm were projected out with any voxels designated as CSF within the radius reassigned as skull (or brain depending on the scenario) with all other layers left untouched. Hence, in one scenario the skull is increased in volume by varying amounts at one point with the brain unchanged while in the other scenario the opposite is the case. Removal of the full thickness of CSF at a given point resulted in an AI of approximately 6%. The increase in skull (or brain) tissue (with reciprocal decrease in CSF) for the different deviation models are shown in Table II, with the quantitative results (only the GMI metric for brevity) shown in Fig. 7.

The results indicate that the BFSD-EIT technique is very sensitive to deviations in anatomy. The replacement of CSF on the LHS by either skull or brain effectively places a low conductivity target at that location with even the smallest radius sphere (resulting in $< 1 \text{ cm}^3$ tissue imbalance on the LHS) compromising results compared to the ideal model. If ROIs are detected, they correspond to the excess skull or brain, meaning that no lesion is detectable.

It is noted, however, that the GMI for a given lesion case is the arithmetic sum of the GMI for the erroneous N case and the GMI for the ideal lesion case. This finding may give the algorithm a degree of robustness to anatomical deviations, as will be discussed in more detail in section IV, E.

2) Altered Boundary- Shrunk and Dilated Scalp

Two fine meshes were developed where the scalp layer was

TABLE II
VOLUME OF THE INCREASE IN SKULL OR BRAIN LAYER (WITH RECIPROCAL DECREASE IN CSF LAYER) ON THE LHS WITH VARYING SPHERE RADII.

Sphere Radius	Volume Increase of Skull		Volume Increase of Brain	
mm	cm ³	% of Total Voxels	cm ³	% of Total Voxels
0	0	0	0	0
10	0.86	0.06	0.84	0.06
20	3.70	0.17	3.56	0.17
50	24.67	1.14	24.35	1.12

shrunk or dilated to 97% and 105% respectively of the original volume. The electrode positions were then translated onto the new boundaries. No other layers were affected. The 97% value represented a shrinking factor that maintained a layer of scalp over the skull (any further reduction in volume resulted in skull layer being exposed to the exterior). The 105% value was chosen as a complementary dilation factor. The work of [36] demonstrated that the external geometry of the head varies between people with various models predicting head circumference based on height and weight and an inter-model variance of about 10%. Hence assuming a “best guess” generic head mesh based on a patient’s height and weight would be available for reconstruction purposes, a 97% - 105% variance in volume should be achievable. The results from these models, shown in Fig. 8, are comparable to the results from the ideal model.

The magnitude of the GMI are greater for the 97% model and less for the 105% model compared to ideal due to the reduction and dilation in scalp volume rendering the perturbations “bigger” and “smaller” compared to the whole head compared to ideal. The IN, MD and DCL metrics are all larger in value (but comparable) to ideal. The RDR is perfect in all cases (0%

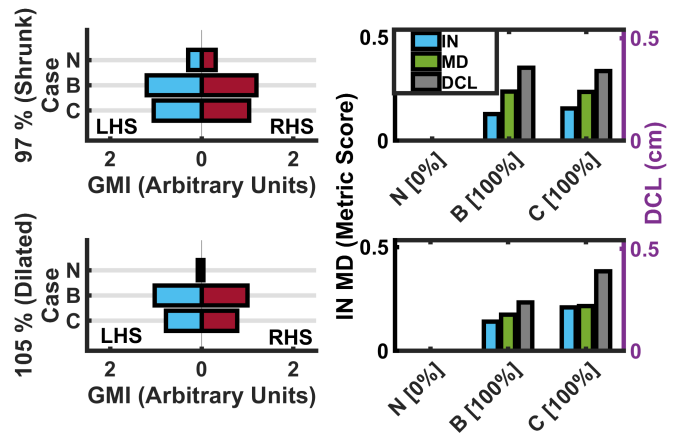


Fig. 8. Quantitative Metrics for models where the scalp layer is shrunk to 97% of the original volume (top row) and dilated to 105% of the original volume (bottom row). Cases are N (no lesion present); B (bleed); C (clot). GMI: The blue bars represent a negative intensity value and the red bars a positive intensity value on either the LHS (negative x-axis) or RHS (positive x-axis). IN, MD and DCL: Are reported if ROIs are detected. The RDR for each case is reported on the x-axis of the IN, MD, DCL plot.

for N, 100% for B,C). Therefore, this result suggests that the BFS-D-EIT algorithm can tolerate small variances in (symmetric) head circumferences.

G. A Frequency-Dependent Background

The disambiguation step of BFS-D-EIT is dependent on a difference in the pattern of conductivity contrast between the bleed or clot and brain at the two different f points. At a f_1 of 25 Hz the conductivities of brain, clot and bleed are 0.1 S/m, 0.05 S/m and 0.7 S/m respectively. Re-application of the algorithm at a f_2 of 100 Hz where these respective tissue conductivities are 0.1 S/m, 0.09 S/m and 0.7 S/m, will result in theoretically identical metrics for a bleed (as the contrast does not change) while for a clot the decrease in contrast will result in metrics more like a normal case [19]. Hence disambiguation is achieved, aided by the assumed frequency-independent brain background.

This section investigates whether disambiguation is possible if the conductivity of brain also changes from f_1 to f_2 , and the change in contrast patterns are similar for lesion types. To investigate this, the GMI for the three cases (i.e., normal, bleed present, and clot present) was computed for a f_1 of 25 Hz and then a f_2 of 25 kHz where the conductivity of brain, bleed and clot are 0.13 S/m, 0.7 S/m and 0.11 S/m as shown in Fig. 1. Crucially the brain conductivity has changed, and the contrast for both clot and bleed with respect to brain is less at f_2 compared to f_1 . The results are shown in Fig. 9. For both lesion cases, the GMI metric decreases in magnitude from f_1 to f_2 as both lesion types have decreased in contrast with respect to brain. Although the scale of decrease is more for clot than bleed, the fact that both decrease confounds disambiguation.

In order to achieve disambiguation, therefore, the selection of f points can be improved. For example, f_1 of 25 Hz and f_2 of 100 Hz, as suggested in [19], could be chosen due to the differing patterns in contrast change for bleed and clot with respect to brain.

However, a more robust technique would be a multi-frequency approach where the overall contrast pattern over a series of points can be used to identify the lesion type. In Fig. 10, the GMI patterns for the three cases over 4 frequency points from 25 Hz to 100 Hz is plotted (the band of most significant conductivity change). The results show that the GMI on both sides are equal but opposite at a given f point and importantly the pattern for a given case mirror the contrast between lesion and background across the band. The GMI of case N is near zero and approximately constant, for B the GMI is large in

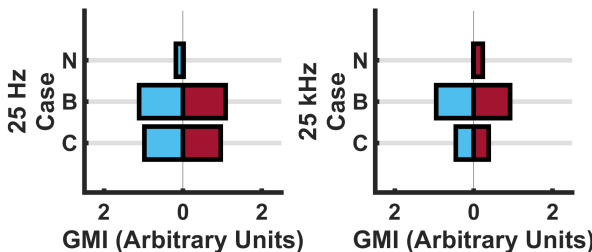


Fig. 9. GMI metric results for the 3 cases at f_1 of 25 Hz and then a f_2 of 25 kHz, demonstrating the effect of a frequency-dependent background.

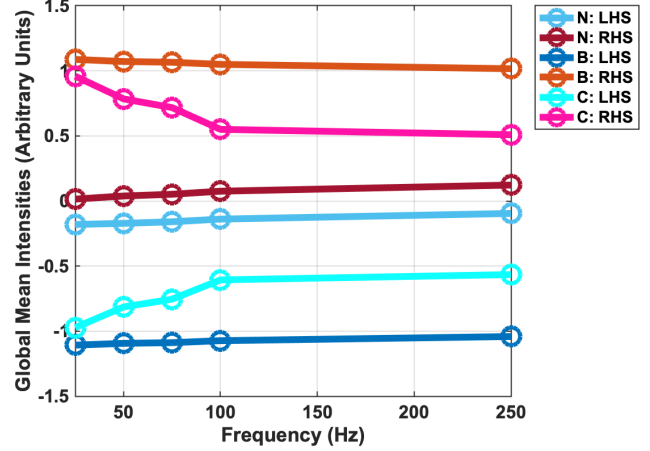


Fig. 10. GMI metric results (LHS and RHS) for the 3 cases (N, B, C) across the 25 Hz – 100 Hz band.

magnitude with a slow decrease across the band as the conductivity of brain slowly increases to reduce the contrast between the brain and the bleed, and case C shows a significant reduction in magnitude of GMI from 25-100 Hz mirroring the reduction in contrast between clot and brain across that frequency range.

H. Application to Human Data

As a final test, the BFS-D-EIT algorithm was applied to human data collected from stroke patients as part of a clinical trial with the Hyper Acute Stroke Unit (HASU) at University College London Hospital (UCLH) [37]. The SNR of the data was approximately 48 dB. A patient was selected with a right-sided ischemic lesion occupying 13.7% of the brain volume ('P26' in the dataset). The measurement frames collected from this patient were reconstructed onto a coarse mesh derived from neuroimaging from the patient (mesh 'A'), and also onto two other meshes derived from two other randomly selected patients 'P9' and 'P11' (meshes 'Y' and 'Z' respectively). This approach was performed to compare the effect of patient specific and non-patient specific meshes on the result. Further, as the measurement frames are from a human patient, the 'forward model' is of a real human head inclusive of complete anatomy and inherent asymmetries. The results are shown in Fig. 11, as the GMI at four points in the 5 Hz – 100 Hz band (corresponding to the f points used in [37]). Noise free simulated measurement frames generated using fine FEM models of the lesion and head from patient P26 were reconstructed onto mesh A and used to represent the 'ideal' result, shown as trace C on Fig. 11.

The results for reconstruction using the patient data and the patient specific mesh A is the nearest to the ideal of trace C, with a high magnitude GMI at the lower end of the band reducing over the band to 100 Hz. Further, for trace A the sign of the GMI matches at all points (positive on the RHS, and negative on the LHS) that of trace C. When reconstruction is performed onto the non-specific meshes, the result deviate from the ideal result. For the reconstruction onto mesh Y, the GMI sign of trace Y match trace C but the reduction in magnitude of GMI across the band is less. For the reconstruction onto mesh Z, the rate of reduction of magnitude is similar to trace A but the GMI sign is opposite (i.e. the clot is detected on the wrong

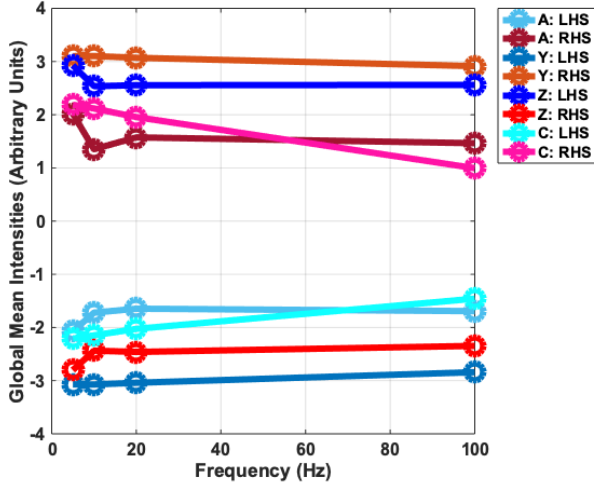


Fig. 11. GMI metric results (LHS and RHS) for human ischaemic stroke patient across the 5 Hz – 100 Hz band. Reconstruction is performed onto a patient specific mesh (A), and two patient non-specific meshes (Y and Z). The results from using simulated data onto the patient specific mesh is also shown (C).

side). The trend in GMI reduction associated with a clot across the band hence appears in both patient specific and non-patient specific meshes, with better results in the patient specific case.

IV. DISCUSSION

A. Measurement Frame Noise

Algorithm performance is unsurprisingly better at higher SNR levels. The results suggest a SNR of 80 dB or higher is required for accurate lesion detection, while application of BFS-D-EIT for stroke detection is still feasible down to an SNR limit of about 60 dB. Beyond this SNR level, degradation of results means lesion detection is not reliable, but is possible as seen with the results from the human patient where measurement frames at 48 dB were used albeit with a large lesion with the results comparable to the equivalent simulated lesion as shown in Fig. 11. While some EIT applications may be feasible at lower SNR levels, use of EIT applied to more demanding neural applications that may involve smaller changes and issues such as the skull and CSF dampening signals generally require systems capable of 80 dB and higher [38]–[41]. It should be noted that the nominal rating of a system is usually higher than that achieved with patients. For example, the human data was recorded using the Scousetom system with a SNR rating of 77.5 dB [39]. Hence as well as improvements in hardware, tackling of other noise sources such as wires, electrodes, and connections will be needed in order to improve the quality of data recorded from patients.

B. Electrode Positioning Errors

EIT is sensitive to errors in electrode positioning [14], with inaccurate electrode positions a major cause of artefacts due to the ill-posed nature of the reconstruction problem [11]. BFS-D-EIT assumes symmetric placement of electrode pairs. Moreover, these placement positions are assumed to be in agreement with the ideal model. These assumptions led to the investigation of the effect of two related potential error sources

in BFS-D-EIT.

1) Electrode Positioning Errors with Symmetry Lost

In this case, electrode pairs are not symmetric with respect to each other and are not correctly positioned relative to the ideal model. A severe effect on algorithm performance is seen in this situation with BFS-D-EIT tolerant to errors in electrode positioning within only a ± 1 mm radius of the positions expected by the ideal model. Unreliable ROI detection with a steep decline in RDR from ideal is seen at radii beyond ± 1 mm. The GMI metric is more robust (reliable up to about ± 5 mm error radius).

2) Electrode Positioning Errors with Symmetry Maintained

In this case, symmetry between electrode pairs is maintained despite incorrect positioning with respect to the ideal model. The results are found to be improved relative to the case in which electrode pairs are not ideally symmetric. The robustness of the GMI is evident with reliable results of up to ± 30 mm error radius, while acceptable results up to only ± 5 mm is achievable for the other metrics (with no or erroneous ROIs detected beyond this).

While the ± 30 mm limit is encouraging, it is only applicable if symmetry between electrode pairs is maintained. Without this condition being achieved the ± 5 mm value is a limitation, however this tolerance is still an order of magnitude of that achieved in [18]. Nevertheless, techniques to improve electrode placement accuracy are essential in order to further improve the robustness of the algorithm. The electrode positioning used is largely based on the EEG 10-20 system, and as such EEG caps may be used in the first instance to aid electrode positioning with a specific hat for BFS-D-EIT a possible improvement [19]. Other aids include the use of image guidance technology [42], automated algorithms to calculate EEG positions [43], and devices to generate quick, precise 3D models of patients' heads for use in EEG electrode placement [44]. Hence, electrode positioning while a challenge for EIT may be one that is surmountable.

C. Contact Impedance Errors of Electrodes

Changes in the electrode contact impedance have little or no effect on the BFS-D-EIT algorithm performance. Notably, the contact impedance ranges chosen ($\pm 20\%$ and $\pm 50\%$ of the ideal value) correspond to suboptimal and unacceptable variances in impedance as described by [18]. Therefore, realistically, variations in contact impedance will be below these ranges and are thus unlikely to impact the algorithm outcomes. As further explained in [18], changes in the impedance of the electrode have little effect on the current flow pattern within the head as the conductivity of the electrode is large (even with the modelled errors) compared to that of the tissues of the head.

D. Assumed Conductivity Errors of the Tissues

The uncertainty and variability in conductivity values of tissues, especially in the EIT range [30], [33] means that the algorithm must be robust to errors in this parameter both at the

voxel and whole tissue levels.

At the voxel level, assigning each voxel a value of the ideal conductivity value for the respective tissue with an error of up to $\pm 0 - 50\%$ had little or no effect on the result compared to ideal. This result is attributed to the reconstruction onto a coarse mesh which has approximately 1/16 the number of voxels compared to the fine mesh. This ‘averages out’ the heterogeneous nature of the tissue voxels in the erroneous models.

At the whole tissue level, assigning each tissue a value of the ideal conductivity value for the respective tissue with an error of up to $\pm 0 - 20\%$ had little effect on the result compared to ideal. The reason for this result is the differencing of measurement frames from symmetrically opposite orientations resulting in error suppression and the contrast (proportional to the difference) between the tissues largely being maintained despite errors in assumed conductivity. Lesion detection is still achieved but the GMI results for the two different lesions are similar for an error of $\pm 0 - 50\%$. As lesion detection is the goal of the algorithm at a single f point (identification of lesion type requiring the disambiguation step as described in [19]), this convergence of values for both cases is not of concern as the pattern of contrast change will differ for the two lesions between f points allowing disambiguation.

Overall, at both voxel and tissue levels, these results are significant. As the true conductivity of a tissue is uncertain, the fidelity of the algorithm even with variability in tissue conductivity of up to 50% is strongly encouraging.

E. Errors in Assumed Anatomy of the Head

Two scenarios were examined with geometries different to that of the coarse reconstruction FEM mesh: (1) unilateral excess of skull or brain, and (2) altered boundary of the head.

1) Unilateral Excess of Skull or Brain

In the first scenario, which examines the unilateral excess of tissues, the effect of reassigning the CSF as skull or brain on the left side is effectively the thickening of the skull (or brain) with a reciprocal thinning of the CSF. At the chosen f point, this modification effectively places a low conductivity target on the LHS compared to the RHS as the conductivity of skull (0.05 S/m) or brain (0.1 S/m) is less than that of CSF (2 S/m). The presence of this low conductivity LHS target compared to the CSF in the symmetric RHS location is seen in the GMI with high intensity on the LHS, low intensity on the RHS (equal but opposite) with the magnitude of the values increasing as the volume of skull (or brain) tissue increases. The results are near identical for both sets of models, however the magnitude of the values from the skull models are slightly larger than those of the brain models as the contrast between skull (0.05 S/m) and CSF (2 S/m) is larger than that between brain (0.1 S/m) and CSF (2 S/m).

In terms of the metrics based on ROIs, the isolation of the largest candidate ROIs results in the excessive skull (or brain) ‘lesion’ being detected instead of the bleed or clot in all cases. In the smallest 10 mm radius model, the lesion is removed by the filtering (too near to the exterior) resulting in no ROI

detection. When ROIs are detected the result is (near) identical metrics for all cases in the excess skull (or brain) models. The size of a ROI is a function of the volume of the lesion but also the contrast between the tissues on either side. The contrast between skull (or brain) and CSF results in larger ROIs than those produced for the 50 ml clot or 10 ml bleed (which are both contrasted with brain).

These results indicate that BFSD-EIT is extremely sensitive to asymmetry in normal anatomy with an excess skull or brain tissue of $< 1 \text{ cm}^3$ on one side capable of masking the presence of true lesions. The excess tissue confounds the ROI analysis). However, the GMI results indicate that asymmetric anatomy may be tolerated by BFSD-EIT if results are gathered at multiple frequencies the arithmetic sum property used. At a second f point where the conductivity of the tissues is different, analysis of the results would identify the presence of a lesion based on the known changes in tissue conductivities between the f points selected. For example, at 100 Hz the decreased contrast between brain (0.1 S/m) and clot (0.09 S/m) will result in a noticeable difference in the GMI result for case C at 100 Hz (closer to the N result) compared to 25 Hz where the enhanced contrast of clot compared to brain deviates the GMI result away from the N result more. If the conductivities do not change then disambiguation would not be possible. In the models used, neither skull, bleed nor CSF change in conductivity over the range considered [16], [24] meaning disambiguation of bleed from normal in the presence of asymmetric excess skull would be challenging.

2) Altered Boundary- Shrunk and Dilated Scalp

It is unlikely that a patient-specific mesh would be available in acute stroke cases. However, it would be possible to have a “generic best guess” mesh for reconstruction that approximated the external head geometry based on non-invasive measurables such as, for example, circumference and nasion-inion distance. The shrunk (97% of original volume) and dilated (105% of original volume) scalp models gave strong results comparable to ideal. Of note, the GMI results were greater in magnitude for the 97% model as less scalp results in a larger effective presence of the lesions. The GMI values were smaller in magnitude for the 105% models for the opposite reason. In [45], it was argued that although images reconstructed onto a correct mesh are of superior quality those from using a generic mesh, using the correct mesh did not improve stroke detection rates and thus a generic mesh may be sufficient. For stroke, lesion detection and lesion-type identification are crucial whereas image quality may not be as vital. As such, a generic best guess mesh may be sufficient for the feasibility of BFSD-EIT in this application.

The alterations in boundary studied are a uniform decrease of increase of the geometry of the original boundary. Non-uniform changes in the boundary would result in the challenges discussed in the previous section (unilateral excess of skull or brain) as well as resulting in changes in the symmetry electrode positioning.

F. A Frequency-Dependent Background

A frequency-dependent background has the ability to

confound lesion detection if the pattern of contrast change between the possible lesion types (bleed or clot) and background is the same from f_1 to f_2 . However, if care is taken in the selection of f points then this potential problem can be avoided. In [19], the f points of 25 Hz and 100 Hz are used as there is a significant decrease in contrast between clot and brain at f_1 compared to f_2 , while there is effectively no change in contrast between bleed and brain at the same two f points. An alternative, and more robust method may be to assess the pattern of contrast change at multiple f points across a band, we intend to explore this in future work.

G. Application to Human Data

The BFS-D-EIT algorithm was applied to human data for the first time in this study. The dataset from the UCLH represents the most comprehensive EIT stroke data currently available but also suffers from limitations including an SNR of 48 dB, and uncertainty over error sources such as electrode positioning [37]. Despite this, the use of human data represents measurement frames from a true forward model as opposed to the controlled environment of numerical models used in other parts of the study. As found in Section III-H, the trend in GMI associated with a clot appears in both patient specific and non-patient specific meshes. These important results point to the strong promise of BFS-D-EIT in stroke diagnosis. The results must however be treated with caution as the data was taken from a patient with a large ischemic lesion, and while the results from using non-patient specific meshes were promising, best results were achieved for the mesh modelled on the anatomy of the patient which may not be available in acute scenarios [45]. The results give an indication that BFS-D-EIT may be feasible in true clinical scenarios with the GMI results for the ischemic lesion generally following the expected ideal pattern for a clot, but not yet of adequate diagnostic value with further studies with more patients and algorithm development needed.

H. Technical Remarks

The computer platform used in this study was a machine with a quad-core Intel Core i7-6700K, 48 GB RAM running Ubuntu 16.04, without a GPU. The main software used in model design, reconstruction and analysis was MATLAB coupled with the resources listed in the Appendix and Bash scripts to facilitate automation. The result was ease of versatility in design of deviation models, automation of forward solving and automation of reconstruction and analysis allowing a wide range of models be investigated and iterations be performed.

Forward solving and reconstruction of a given case took approximately 15 minutes and 5 minutes, respectively, with better performance expected if a GPU had been available. We believe this setup, and in particular the novel EIT resources listed in the Appendix, to be a valuable platform to aid in comprehensive and thorough studies involving EIT.

V. CONCLUSION

The BFS-D-EIT algorithm provides some robustness to modelling errors by using a differencing approach (akin to the robustness seen in fdEIT). This study has applied the BFS-D-

EIT algorithm to stroke diagnosis in a variety of realistic numerical simulations. Scenarios designed to test the robustness and limitations of the algorithm have been examined. We conclude:

- The SNR of the measurement system should be at least 60 dB.
- Electrode positioning errors severely effect on performance. However, tolerance of up to ± 30 mm from the expected position is seen if symmetry is maintained between partner electrodes.
- Contact impedance errors of electrodes (up to $\pm 50\%$ of the assumed impedance) have little effect on performance.
- Assumed conductivity errors in tissues (up to $\pm 50\%$ of the reference value) have little effect on performance whether at a voxel or whole tissue level.
- Errors in assumed anatomy affect the performance of the algorithm. Asymmetrical anatomy across the sagittal plane can be detected as false positive lesions and mask true lesions. The GMI metric may be used to overcome this limitation, if the tissues have a frequency-dependent change in conductivity. Errors in the assumed boundary of the head with a 10% variance only slightly decreases performance.
- A frequency-dependent background can confound disambiguation if f points are not carefully chosen. A multi-frequency approach may be a more robust way to deal with frequency-dependent background with assessment of the overall contrast pattern across a band.
- A final absolute limitation of BFS-D-EIT is an inability to detect lesions that lie perfectly across the plane of symmetry due to the basis of the algorithm being detection of differences in symmetry if present [19].

These scenarios encompass common and important challenges of EIT. When compared to the state-of-the-art algorithm involving EIT applied to stroke problem, the fdEIT algorithm [18], BFS-D-EIT compares favorably. BFS-D-EIT shares the same challenges with regards anatomical variation, but shows superior tolerance to electrode positioning errors (errors of 0.5 mm in [18] resulted in failure to detect lesions), while also sharing robustness to contact impedance [18]. BFS-D-EIT shows advantages over the algorithm presented in [18] in terms of computational efficiency. Further, as BFS-D-EIT compares measurement frames at each frequency point from mirror image orientations at that frequency point, it avoids a direct comparison of measurement frames taken at different frequency points. Hence, BFS-D-EIT avoids sources of error associated with fdEIT techniques resulting from the fact that different errors are present at different frequencies [13], [16], [19]. This latter point also explains the superior hemorrhage detection of BFS-D-EIT over a fdEIT algorithm such as that in [18] as in BFS-D-EIT the contrast in conductivity between hemorrhage and brain is leveraged at each f point for detection, and does not rely on a change in conductivity across frequencies which is absent for bleed and brain. Finally, the results in this study were achieved without mesh refinement at electrode contact points which was required in [18]. This lack of electrode refinement aids in the computational efficiency of BFS-D-EIT.

While BFS-D-EIT has limitations and is currently not fit for consideration in clinical use as a stand-alone diagnostic device, the technique shows strong promise when applied to stroke

diagnosis provided that the error tolerances listed above are respected. In particular, use of the GMI metric and a multi-frequency approach can result in a robust stroke detection method with promising results seen in the application of the algorithm to data from a human ischemic stroke patient. Future work will further investigate this algorithm, and examine application optimization when applied to phantom and human data.

APPENDIX

All models and software relating to the head model is available at <https://github.com/EIT-team/Tanks> (archived at DOI:10.5281/zenodo.1489106). The forward solver used, PEITS (Parallel EIT Solver) is available at <https://github.com/EIT-team/PEITS> (archived at DOI: 10.5281/zenodo.1641128), and the reconstruction software is available at <https://github.com/EIT-team/Reconstruction> (archived at DOI: 10.5281/zenodo.1643416).

REFERENCES

- [1] P. M. W. Bath, 'ABC of arterial and venous disease: Acute stroke', *BMJ*, vol. 320, no. 7239, pp. 920–923, Apr. 2000.
- [2] W. J. Powers *et al.*, '2018 Guidelines for the Early Management of Patients With Acute Ischemic Stroke: A Guideline for Healthcare Professionals From the American Heart Association/American Stroke Association', *Stroke*, vol. 49, no. 3, pp. e46–e99, Mar. 2018.
- [3] J. A. Chalela *et al.*, 'Magnetic resonance imaging and computed tomography in emergency assessment of patients with suspected acute stroke: a prospective comparison', *The Lancet*, vol. 369, no. 9558, pp. 293–298, Jan. 2007.
- [4] D. Birenbaum, L. W. Bancroft, and G. J. Felsberg, 'Imaging in acute stroke', *West. J. Emerg. Med.*, vol. 12, no. 1, pp. 67–76, Feb. 2011.
- [5] B. J. Kim *et al.*, 'Magnetic Resonance Imaging in Acute Ischemic Stroke Treatment', *J. Stroke*, vol. 16, no. 3, p. 131, 2014.
- [6] T. Dowrick, C. Blochet, and D. Holder, 'In vivo bioimpedance measurement of healthy and ischaemic rat brain: implications for stroke imaging using electrical impedance tomography', *Physiol. Meas.*, vol. 36, no. 6, pp. 1273–1282, Jun. 2015.
- [7] International Organization for Standardization, 'International Electrotechnical Commission. Medical Electrical Equipment: Part 1: General Requirements for Basic Safety and Essential Performance.' IEC 60601-1, 2002.
- [8] D. Holder and Institute of Physics (Great Britain), Eds., *Electrical impedance tomography: methods, history, and applications*. Bristol; Philadelphia: Institute of Physics Pub, 2005.
- [9] B. Brown, 'Electrical impedance tomography (EIT): a review', *J. Med. Eng. Technol.*, vol. 27, no. 3, pp. 97–108, Jan. 2003.
- [10] A. Boyle and A. Adler, 'The impact of electrode area, contact impedance and boundary shape on EIT images', *Physiol. Meas.*, vol. 32, no. 7, pp. 745–754, Jul. 2011.
- [11] M. Jehl, J. Avery, E. Malone, D. Holder, and T. Betcke, 'Correcting electrode modelling errors in EIT on realistic 3D head models', *Physiol. Meas.*, vol. 36, no. 12, pp. 2423–2442, Dec. 2015.
- [12] E. Malone, G. S. dos Santos, D. Holder, and S. Arridge, 'A Reconstruction-Classification Method for Multifrequency Electrical Impedance Tomography', *IEEE Trans. Med. Imaging*, vol. 34, no. 7, pp. 1486–1497, Jul. 2015.
- [13] E. Malone, G. Sato dos Santos, D. Holder, and S. Arridge, 'Multifrequency Electrical Impedance Tomography Using Spectral Constraints', *IEEE Trans. Med. Imaging*, vol. 33, no. 2, pp. 340–350, Feb. 2014.
- [14] A. Adler and A. Boyle, 'Electrical Impedance Tomography: Tissue Properties to Image Measures', *IEEE Trans. Biomed. Eng.*, vol. 64, no. 11, pp. 2494–2504, Nov. 2017.
- [15] S. Ahn, T. I. Oh, S. C. Jun, J. K. Seo, and E. J. Woo, 'Validation of weighted frequency-difference EIT using a three-dimensional hemisphere model and phantom', *Physiol. Meas.*, vol. 32, no. 10, pp. 1663–1680, Oct. 2011.
- [16] B. Packham *et al.*, 'Comparison of frequency difference reconstruction algorithms for the detection of acute stroke using EIT in a realistic head-shaped tank', *Physiol. Meas.*, vol. 33, no. 5, pp. 767–786, May 2012.
- [17] J. Ma *et al.*, 'Exploratory Study on the Methodology of Fast Imaging of Unilateral Stroke Lesions by Electrical Impedance Asymmetry in Human Heads', *Sci. World J.*, vol. 2014, pp. 1–18, 2014.
- [18] E. Malone, M. Jehl, S. Arridge, T. Betcke, and D. Holder, 'Stroke type differentiation using spectrally constrained multifrequency EIT: evaluation of feasibility in a realistic head model', *Physiol. Meas.*, vol. 35, no. 6, pp. 1051–1066, Jun. 2014.
- [19] B. J. McDermott, J. Avery, M. O'Halloran, K. Y. Aristovich, and E. Porter, 'Bi-frequency symmetry difference electrical impedance tomography – a novel technique for perturbation detection in static scenes', *Physiol. Meas.*, Feb. 2019.
- [20] J. Zhang *et al.*, 'A novel 3D-printed head phantom with anatomically realistic geometry and continuously varying skull resistivity distribution for electrical impedance tomography', *Sci. Rep.*, vol. 7, no. 1, Dec. 2017.
- [21] W. R. B. Lionheart, 'EIT reconstruction algorithms: pitfalls, challenges and recent developments', *Physiol. Meas.*, vol. 25, no. 1, pp. 125–142, Feb. 2004.
- [22] B. Grychtol and A. Adler, 'FEM electrode refinement for electrical impedance tomography', in *2013 35th Annual International Conference of the IEEE Engineering in Medicine and Biology Society (EMBC)*, 2013, vol. 2013, pp. 6429–6432.
- [23] M. Jehl, A. Dedner, T. Betcke, K. Aristovich, R. Kloforn, and D. Holder, 'A Fast Parallel Solver for the Forward Problem in Electrical Impedance Tomography', *IEEE Trans. Biomed. Eng.*, vol. 62, no. 1, pp. 126–137, Jan. 2015.
- [24] L. Horeh, 'Some Novel Approaches in Modelling and Image Reconstruction for Multi-Frequency Electrical Impedance Tomography of the Human Brain', UCL, London, UK, 2006.
- [25] P. Hasgall *et al.*, 'IT'IS Database for thermal and electromagnetic parameters of biological tissues', 2015. [Online]. Available: www.itis.ethz.ch/database. [Accessed: 25-Nov-2016].
- [26] J. B. Fiebach *et al.*, 'Stroke Magnetic Resonance Imaging Is Accurate in Hyperacute Intracerebral Hemorrhage: A Multicenter Study on the Validity of Stroke Imaging', *Stroke*, vol. 35, no. 2, pp. 502–506, 2004.
- [27] S. Payabvash, S. Taleb, J. C. Benson, and A. M. McKinney, 'Acute Ischemic Stroke Infarct Topology: Association with Lesion Volume and Severity of Symptoms at Admission and Discharge', *Am. J. Neuroradiol.*, vol. 38, no. 1, pp. 58–63, Jan. 2017.
- [28] G. Bonmassar, S. Iwaki, G. Goldmakher, L. M. Angelone, J. W. Belliveau, and M. H. Lev, 'On the Measurement of Electrical Impedance Spectroscopy (EIS) of the Human Head', *Int. J. Bioelectromagn.*, vol. 12, no. 1, pp. 32–46, Jan. 2010.
- [29] L. Liu *et al.*, 'A new method of noninvasive brain-edema monitoring in stroke: cerebral electrical impedance measurement', *Neurol. Res.*, vol. 28, no. 1, pp. 31–37, Jan. 2006.
- [30] B. McDermott *et al.*, 'Stable tissue-mimicking materials and an anatomically realistic, adjustable head phantom for electrical impedance tomography', *Biomed. Phys. Eng. Express*, vol. 4, no. 1, p. 015003, Nov. 2017.
- [31] C. Gabriel, 'Dielectric properties of biological tissue: Variation with age', *Bioelectromagnetics*, vol. 26, no. S7, pp. S12–S18, 2005.
- [32] C. Gabriel and A. Peyman, 'Dielectric measurement: error analysis and assessment of uncertainty', *Phys. Med. Biol.*, vol. 51, no. 23, pp. 6033–6046, Dec. 2006.
- [33] C. Gabriel, A. Peyman, and E. H. Grant, 'Electrical conductivity of tissue at frequencies below 1 MHz', *Phys. Med. Biol.*, vol. 54, no. 16, pp. 4863–4878, 2009.
- [34] P. P. Russo and R. L. Smith, 'Asymmetry of Human Skull Base During Growth', *Int. J. Morphol.*, vol. 29, no. 3, pp. 1028–1032, Sep. 2011.
- [35] X.-Z. Kong *et al.*, 'Mapping cortical brain asymmetry in 17,141 healthy individuals worldwide via the ENIGMA Consortium', *Proc. Natl. Acad. Sci.*, vol. 115, no. 22, pp. E5154–E5163, May 2018.
- [36] A. K. D. Nguyen, A. A. Simard-Meilleur, C. Berthiaume, R. Godbout, and L. Mottion, 'Head Circumference in Canadian Male Adults: Development of a Normalized Chart', *Int. J. Morphol.*, vol. 30, no. 4, pp. 1474–1480, Dec. 2012.

- [37] N. Goren *et al.*, ‘Multi-frequency electrical impedance tomography and neuroimaging data in stroke patients’, *Sci. Data*, vol. 5, p. 180112, Jul. 2018.
- [38] T. I. Oh, H. Wi, D. Y. Kim, P. J. Yoo, and E. J. Woo, ‘A fully parallel multi-frequency EIT system with flexible electrode configuration: KHU Mark2’, *Physiol. Meas.*, vol. 32, no. 7, pp. 835–849, Jul. 2011.
- [39] J. Avery, T. Dowrick, M. Faulkner, N. Goren, and D. Holder, ‘A Versatile and Reproducible Multi-Frequency Electrical Impedance Tomography System’, *Sensors*, vol. 17, no. 2, pp. 280–280, Jan. 2017.
- [40] W. Hun, H. Sohal, A. L. McEwan, E. J. Woo, and T. I. Oh, ‘Multi-Frequency Electrical Impedance Tomography System With Automatic Self-Calibration for Long-Term Monitoring’, *IEEE Trans. Biomed. Circuits Syst.*, vol. 8, no. 1, pp. 119–128, Feb. 2014.
- [41] J. Avery, T. Dowrick, A. Witkowska-Wrobel, M. Faulkner, K. Y. Aristovich, and D. S. Holder, ‘Simultaneous EIT and EEG using frequency division multiplexing’, *Physiol. Meas.*, Mar. 2019.
- [42] S. Jeon, J. Chien, C. Song, and J. Hong, ‘A Preliminary Study on Precision Image Guidance for Electrode Placement in an EEG Study’, *Brain Topogr.*, vol. 31, no. 2, pp. 174–185, Mar. 2018.
- [43] P. Giacometti, K. L. Perdue, and S. G. Diamond, ‘Algorithm to find high density EEG scalp coordinates and analysis of their correspondence to structural and functional regions of the brain’, *J. Neurosci. Methods*, vol. 229, pp. 84–96, May 2014.
- [44] G. Bonmassar and S. Iwaki, ‘The Shape of Electrical Impedance Spectroscopy (EIS) is altered in Stroke Patients’, in *The 26th Annual International Conference of the IEEE Engineering in Medicine and Biology Society*, San Francisco, CA, USA, 2004, vol. 4, pp. 3443–3446.
- [45] M. Jehl, K. Aristovich, M. Faulkner, and D. Holder, ‘Are patient specific meshes required for EIT head imaging?’, *Physiol. Meas.*, vol. 37, no. 6, pp. 879–892, Jun. 2016.